

# Referenceless Prediction of Perceptual Fog Density and Perceptual Image Defogging

Lark Kwon Choi, *Member, IEEE*, Jaehee You, and Alan Conrad Bovik, *Fellow, IEEE*

**Abstract**—We propose a referenceless perceptual fog density prediction model based on natural scene statistics (NSS) and fog aware statistical features. The proposed model, called Fog Aware Density Evaluator (FADE), predicts the visibility of a foggy scene from a single image without reference to a corresponding fog-free image, without dependence on salient objects in a scene, without side geographical camera information, without estimating a depth-dependent transmission map, and without training on human-rated judgments. FADE only makes use of measurable deviations from statistical regularities observed in natural foggy and fog-free images. Fog aware statistical features that define the perceptual fog density index derive from a space domain NSS model and the observed characteristics of foggy images. FADE not only predicts perceptual fog density for the entire image, but also provides a local fog density index for each patch. The predicted fog density using FADE correlates well with human judgments of fog density taken in a subjective study on a large foggy image database. As applications, FADE not only accurately assesses the performance of defogging algorithms designed to enhance the visibility of foggy images, but also is well suited for image defogging. A new FADE-based referenceless perceptual image defogging, dubbed DENSITY of Fog Assessment-based DEFogger (DEFAGE) achieves better results for darker, denser foggy images as well as on standard foggy images than the state of the art defogging methods. A software release of FADE and DEFAGE is available online for public use: <http://live.ece.utexas.edu/research/fog/index.html>.

**Index Terms**—Fog, perceptual fog density, defog, dehazing, visibility enhancement, natural scene statistics.

## I. INTRODUCTION

THE perception of outdoor natural scenes is important for understanding the natural environment and for successfully executing visual activities such as object detection, recognition, and navigation [1]. In bad weather, the absorption or scattering of light by atmospheric particles such as fog, haze, or mist can greatly reduce the visibility of scenes [2]. As a result, objects in images captured under

bad weather conditions suffer from low contrast, faint color, and shifted luminance. Since the reduction of visibility can dramatically degrade operators' judgments in vehicles guided by camera images and can induce erroneous sensing in remote surveillance systems, automatic methods for visibility prediction and enhancement of foggy images have been intensively studied.

Current visibility prediction models that operate on a foggy image require a corresponding fog-free image of the same scene taken under different weather conditions to compare visibility, or identified salient objects in a foggy image such as lane markings or traffic signs to supply distance cues [3]. Multiple foggy images of the same scene [2] or obtained by different degrees of polarization by rotating polarizing filters attached to a camera [4] have also been used. However, attaining enough images is time-consuming, and it is difficult to find the maximum and minimum degree of polarization during rapid scene changes. Hautière *et al.* [5] presented an automatic method of fog detection and of estimation of visibility distance using side geographical information obtained from an onboard camera. While this method avoids the need for multiple images, it is still difficult to apply in practice because creating accurate 3D geometric models that can capture dynamic real-world structure is challenging. In addition, this approach works only under limited assumption, e.g., on moving vehicles, so it is not necessarily applicable to general foggy scenes.

Regarding visibility enhancement of foggy images, diverse defogging models have been proposed. The earliest approaches utilized a dark-object subtraction method to handle atmospheric scattering correction of multispectral data [6] or multiple images of the same scene under different weather conditions [1], [2], [4]. Later, approximate 3D geometrical models of the scene were used. For example, Hautière *et al.* [7] proposed a fog-free in-vehicle vision system using contrast restoration, while Kopf *et al.* [8] introduced the Deep Photo system utilizing existing georeferenced digital terrain and urban models to improve the visibility of foggy images. A more efficient and desirable approach is to use only a single foggy image; however, direct prediction of fog density from a single foggy image is difficult. Therefore, most defogging algorithms utilize an additional estimated depth map or a depth dependent transmission map to improve visibility using assumptions from, e.g., Koschmieder's atmospheric scattering model [9]. Tan [10] predicted scene albedo by maximizing local contrast while supposing a smooth layer

Manuscript received November 28, 2014; revised April 7, 2015; accepted June 22, 2015. Date of publication July 15, 2015; date of current version July 30, 2015. This work was supported by the Business for Cooperative Research and Development between Industry, Academy, and Research Institute through the Korea Small and Medium Business Administration in 2013 under Grant C0014365. The associate editor coordinating the review of this manuscript and approving it for publication was Prof. Damon M. Chandler.

L. K. Choi and A. C. Bovik are with the Department of Electrical and Computer Engineering, The University of Texas at Austin, Austin, TX 78712 USA (e-mail: larkkwonchoi@utexas.edu; bovik@ece.utexas.edu).

J. You is with the Department of Electronic and Electrical Engineering, Hongik University, Seoul 121-791, Korea (e-mail: jaehee@hongik.ac.kr).

Color versions of one or more of the figures in this paper are available online at <http://ieeexplore.ieee.org>.

Digital Object Identifier 10.1109/TIP.2015.2456502

of airlight, but the results tended to be overly saturated creating halo effects. Fattal [11] improved visibility by assuming that transmission and surface shading are statistically uncorrelated. However, this method requires substantial color and luminance variation to occur in the foggy scene. He *et al.* [12] made the important contribution of the *dark channel prior*. Deploying this constraint delivers more successful results by refining the initial transmission map using a soft matting method; however, soft matting is computationally expensive, although it can be sped up using a guided filter [13]. Tarel and Hautière [14] built a fast solution using an edge preserving *median of median filter*, but the extracted depth-map must be smooth except along edges that are coincident with large depth jumps. Kratz and Nishino [15] and Nishino *et al.* [16] suggested a Bayesian defogging model that jointly predicts the scene albedo and depths based on a factorial Markov random field. Results are generally pleasing, but this technique produces some dark artifacts at regions approaching infinite depth.

Recently, Ancuti and Ancuti [17] used multiscale fusion [18], [19] for single image dehazing. Image fusion is a method to blend several images into a single one by retaining only the most useful features. Dehazing by multiscale fusion has advantages: it can reduce patch-based artifacts by single pixel operations, and it is fast since it does not predict a transmission map. Still, the design of methods of image preprocessing and weight maps from only a single foggy image without other references such as a corresponding fog-free image or side geographical information remains difficult. Ancuti *et al.* derived a method of image preprocessing whereby the average luminance of a single foggy image is subtracted, then the result is magnified. This method can capture rough haze regions and restore visibility on many foggy images. However, the performance is lowered when the foggy images are dark or the fog is dense because severe dark aspects of the preprocessed image begin to dominate. Although introducing weight maps can help mitigate the degradation, the visibility is not enhanced much.

In addition, Gibson and Nguyen [20] provided an aggregate contrast enhancement metric that was trained using low-level contrast enhancement metrics and human observations to solve the problem of enhancing foggy images of ocean scenes. Although the metric performance is improved, this kind of training based metric is necessarily limited, since it can only capture and assess contrast degradations arising from the images that it has been trained on, particularly images of foggy ocean scenes. Hence, training-free visibility enhancement is of great interest.

Early on, the performance of defogging algorithms has only been evaluated subjectively due to the absence of any appropriate visibility assessment tool. In general, humans are regarded as the ultimate arbiters of the quality or appearance of visual signals [21], so the most accurate way to evaluate any defogging algorithm is to obtain human judgments of the visibility and enhanced quality of defogged images. However, human subjective assessments are laborious, time consuming, non-repeatable, and are not useful for large, remote, or mobile data. These limits have led researchers to develop

objective performance assessment methods for defogging algorithms. Recently, gain parameters indicating newly visible edges, the percentage of pixels that become black or white after defogging, and the mean ratio of the gradients at visible edges have been compared before and after defogging processes [22]. Objective image quality assessment (IQA) algorithms have also been used to evaluate the enhanced contrast and the structural changes of a defogged image [23], [24]. However, these comparison methods require the original foggy image as a reference to evaluate the defogged image. Moreover, existing IQA metrics are generally inappropriate for this application since they are designed to assess distortion levels rather than the visibility of foggy images which may not be otherwise distorted. Hence, no-reference (NR) and defogging-purposed generic visibility evaluation tools are desirable goals.

There does not yet exist a referenceless perceptual fog density prediction model that has been shown to consistently correlate well with human judgments of fog density. This is an important problem, since most captured images are intended for human consumption. While not always necessary, often it would be desirable to be able to automatically assess and reduce fog in a perceptually agreeable manner. Towards achieving perception-driven accurate visibility prediction, we have developed a new model dubbed *Fog Aware Density Evaluator* (FADE) based on models of NSS and fog aware statistical features. As compared with previous methods [1]–[5], the proposed model has clear advantages. Specifically, FADE can predict visibility on a foggy scene without reference to a corresponding fog-free image, without multiple foggy images, without any dependency on pre-detected salient objects in a foggy scene, without side geographical information obtained from an onboard camera, without estimating a depth dependent transmission map, and without training on human-rated judgments. FADE only utilizes measurable deviations from statistical regularities observed on natural foggy and fog-free images. The fog aware features that define the perceptual fog density predictor were validated on a corpus of 500 foggy images and another collection of 500 fog-free images. The features are derived from a reliable space domain NSS model [25], [26] and on observed characteristics of foggy images including low contrast, faint color, and shifted luminance.

The space domain NSS model involves computing local mean subtracted, contrast normalized (MSCN) coefficients of natural images [26]. Models of the distributions of the MSCN coefficients and of the pairwise products of neighboring MSCN coefficients along vertical orientations are used to derive fog aware statistical features. Other fog aware features are derived from the local mean and the local coefficient of variance for sharpness [27], the contrast energy [28], the image entropy [29], the pixel-wise dark channel prior [12], [23], the color saturation, and the colorfulness [30]. A total of 12 local fog aware statistical features are computed on each  $P \times P$  partitioned image patch. A Multivariate Gaussian (MVG) [31] model of the aggregated feature set is then invoked to predict the fog density of a test foggy image by using a Mahalanobis-like distance measure between the MVG fit of

the fog aware statistical features from the test image and the MVG model obtained on natural foggy and fog-free images, respectively.

To evaluate the performance of FADE, a human subjective study was performed using another, content-separate corpus of 100 foggy images. Results show that the perceptual fog density predicted by FADE correlates well with human judgments of fog density on a wide variety of foggy images.

As powerful applications, FADE can accurately evaluate the performance of defogging algorithms by predicting perceptual fog density of the defogged image, and can be used to construct image defogging models designed to enhance the visibility of foggy images. We validate the possibility of FADE as a NR tool to assess the performance of defogging algorithms by comparing the predicted fog density of the defogged images against perceived fog density reported by human observers. To achieve image defogging, we also developed a referenceless perceptual image defogging algorithm, dubbed *DEnsity of Fog Assessment-based DEfogger* (DEFADE). Here, *referenceless* means that the proposed model does not require multiple foggy images, different degrees of polarization, salient objects in a foggy scene, side geographical information, a depth dependent transmission map, training on human judgments, or content assumptions such as smoothness of airlight layers, smoothness of a depth map, or the existence of substantial variations of color in a foggy scene [32]. DEFADE achieves better results on darker, denser foggy images as well as on standard test foggy images than top performing defogging methods, as determined by subjective and objective evaluations.

## II. BACKGROUND

### A. Optical Model of Foggy Image

1) *Foggy Image Formation*: Accurate modeling of optical scattering is a complex problem that is complicated by the wide variety of types, sizes, orientations, and distributions of particles constituting a media, as well as the wavelength direction of the ambient incident light, and the polarization states of the light [2]. Thus, the simplified Koschmieder atmospheric scattering model [9] has been widely used to explain optical foggy image formation.

When solar light passes through a foggy atmosphere, light reflected from objects is directly attenuated along the path to the camera and also diffusely scattered. Mathematically, a foggy image  $I$  may be decomposed into two components, direct attenuation and airlight, as follows,

$$I(x) = J(x)t(x) + A[1 - t(x)], \quad (1)$$

where  $J(x)$  is the scene radiance or a fog-free image to be reconstructed at each pixel  $x$ ,  $t(x) \in [0, 1]$  is the transmission of the reflected light in the atmosphere, and  $A$  is the global skylight that represents ambient light in the atmosphere. The first term  $J(x)t(x)$  is direct attenuation indicating how the scene radiance is attenuated by the medium. The second term,  $A[1 - t(x)]$  called airlight, arises from previously scattered light, which can cause a shift in scene color. In general, by assuming that the atmosphere is homogenous and that light

traveling a longer distance is more attenuated and scattered,  $t(x)$  can be expressed as  $t(x) = \exp[-\beta d(x)]$ , where  $\beta$  is the attenuation coefficient of the medium, and  $d(x)$  is the distance between the scene and the observer.

2) *Characteristics of Foggy Images*: The simplified Koschmieder atmospheric scattering model can be used to explain the observable characteristics of foggy images such as low contrast, faint color, and shifted luminance [10], [33]. A good measure of the image contrast

$$C_{edges}[I(x)] = \sum_{c,x} |\nabla I_c(x)|, \quad (2)$$

where  $c \in \{R, G, B\}$  are *RGB* channels, and  $\nabla$  is the gradient operator. This equation implies that an image of higher contrast produces more sharp edges. The contrast of a foggy image  $I(x)$  where  $t(x) = t < 1$  can be expressed:

$$\begin{aligned} C_{edges}[I(x)] &= \sum_{c,x} |t \nabla J_c(x) + (1-t) \nabla A| = \sum_{c,x} |t \nabla J_c(x)| \\ &< \sum_{c,x} |\nabla J_c(x)| = C_{edges}[J(x)]. \end{aligned} \quad (3)$$

Following (3), the contrast of foggy scenes is generally lower than that of fog-free scenes.

If we assume that the fog in the scenes equally scatters each visible wavelength (although not necessarily true), e.g., the red (*R*), green (*G*), and blue (*B*) channels captured by most camera sensors, then every pixel of each *RGB* color channel can be presumed to have the same depth,  $t(x) = t$ , and the value of  $A$  between color channels to differ little.<sup>1</sup> Then, the color of a foggy image tends to be fainter than that of a fog-free image, increasing with scene depth. This can be expressed as

$$\lim_{d \rightarrow \infty} \frac{|I_i(x) - I_j(x)|}{|J_i(x) - J_j(x)|} \approx \lim_{d \rightarrow \infty} e^{-\beta d(x)} = 0, \quad (4)$$

where  $i, j \in \{R, G, B\}$  represents *RGB* channels.

Since we may assume that the global skylight  $A$  is larger than the intensity of  $I$ , and that when  $0 < t(x) < 1$ , the luminance of foggy scenes is larger than that of fog-free scenes, then

$$\begin{aligned} A - I(x) &= [A - J(x)]t(x) > 0, \\ I(x) - J(x) &= [A - J(x)][1 - t(x)] > 0. \end{aligned} \quad (5)$$

### B. Natural Scene Statistics in the Spatial Domain

The regularity of NSS has been well established in the vision science literature [34], [35]. In the spatial domain, Ruderman [25] observed that removing local mean displacements from natural images and normalizing the local variance of the resulting debiased images has a decorrelating and gaussianizing effect. Divisive normalization also mimics the contrast-gain mechanism in visual cortex [36], [37]. In [26], such an operation was applied to yield

<sup>1</sup>In the future, although we have not done so here, it may be fruitful to relax the assumption of equal scattering across wavelengths.

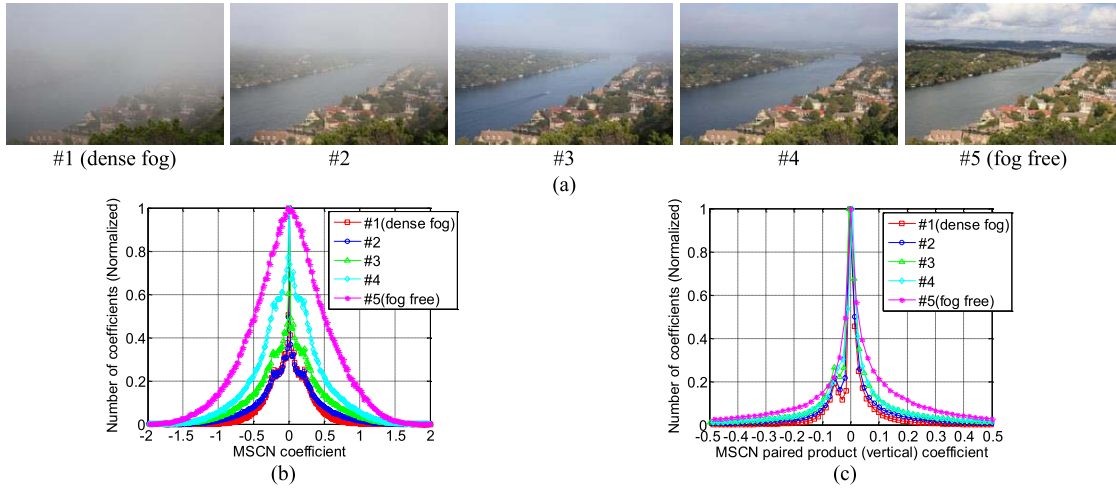


Fig. 1. Histogram of MSCN coefficients: (a) Natural foggy images afflicted by various fog levels. Image #1 shows dense fog, while image #5 is fog-free. (b) Histogram of MSCN coefficients for images shown in (a). (c) Histogram of MSCN paired product (vertical) coefficients for images shown in (a).

MSCN coefficients as follows,

$$I_{\text{MSCN}}(i, j) = \frac{I_{\text{gray}}(i, j) - \mu(i, j)}{\sigma(i, j) + 1}, \quad (6)$$

$$\begin{aligned} \mu(i, j) &= \sum_{k=-K}^K \sum_{l=-L}^L \omega_{k,l} I_{\text{gray}}(i+k, j+l), \\ \sigma(i, j) &= \sqrt{\sum_{k=-K}^K \sum_{l=-L}^L \omega_{k,l} [I_{\text{gray}}(i+k, j+l) - \mu(i, j)]^2}, \end{aligned} \quad (7)$$

where  $i \in \{1, 2, \dots, M\}$ ,  $j \in \{1, 2, \dots, N\}$  are spatial indices,  $M$  and  $N$  are the image dimensions,  $\omega = \{\omega_{k,l} | k = -K, \dots, K, l = -L, \dots, L\}$  is a 2D circularly symmetric Gaussian weighting function sampled out to 3 standard deviations ( $K = L = 3$ ) and rescaled to unit volume.  $I_{\text{gray}}$  is the gray version of a natural image  $I$ . For natural images, the MSCN values are close to unit-normal Gaussian and highly decorrelated, while the MSCN of distorted images tend away from Gaussian and can contain significant spatial correlation. Products of adjacent MSCN coefficients of natural images also exhibit a regular structure, whereas distorted images disturb the regularity [26].

### III. PREDICTION MODEL OF PERCEPTUAL FOG DENSITY

The referenceless prediction model of perceptual fog density FADE extracts fog aware statistical features from a test foggy image, fits fog aware features to a MVG model, then computes deviations from the statistical regularities observed on natural foggy and fog-free images. The fog aware statistical features are derived using a space domain regular NSS model and the characteristics of foggy images. Deviations are computed using a Mahalanobis-like distance measure between the MVG fit of the fog aware features obtained from the test image against an MVG model of fog aware features

extracted from a corpus of 500 fog-free images and another corpus of 500 foggy images, respectively. Each corresponding distance is defined as a foggy level and a fog-free level. The perceptual fog density is then expressed as the ratio of the foggy level to the fog-free level. The ratio method embodies statistical features from both foggy and fog-free images, and thereby is able to predict perceptual fog density over a wider range than using foggy level alone. Each stage of processing is detailed in the following.

#### A. Fog Aware Statistical Features

The first three fog aware statistical features are derived from local image patches. The essential low order statistics of foggy and fog-free images, which are perceptually relevant, are extracted from a spatial domain NSS model of local MSCN coefficients. For natural foggy images, we have found that the variance of the MSCN coefficients decreases as fog density increases [38], as shown in Fig. 1(b). The relative spreads of the empirical densities of the pairwise products of neighboring MSCN coefficients along the vertical orientation also exhibit a regular structure on the right and left sides of the mode, respectively, as shown in Fig. 1(c). Hence, we use the variance of the MSCN coefficient histograms, and the left and right spread parameters of the pairwise products of neighboring MSCN coefficients along the vertical direction as fog aware features for each patch. While it is possible to compute product statistics along more orientations, this does not contribute much to the performance of our model, owing to the isotropic nature of fog. Vertical pairwise product [26] is obtained as follows:

$$I_{\text{Vpair\_MSCN}}(i, j) = I_{\text{MSCN}}(i, j) \cdot I_{\text{MSCN}}(i+1, j). \quad (9)$$

Other fog aware statistical features are derived from the observed characteristics of foggy images such as low contrast, faint color, and shifted luminance by measuring the local sharpness [27], the coefficient of variation of sharpness, the contrast energy [28], the image entropy [29], the pixel-wise

dark channel prior [12], [23], the color saturation in *HSV* color space, and the colorfulness [30].

The local standard deviation  $\sigma(i, j)$  in (8) is a significant descriptor of structural image information that quantifies local sharpness. However, the perceptual impact of  $\sigma(i, j)$  varies with the local mean value  $\mu(i, j)$ . Hence, the coefficient of variation,

$$\xi(i, j) = \frac{\sigma(i, j)}{\mu(i, j)}, \quad (10)$$

which measures the normalized dispersion, is computed. Both  $\sigma(i, j)$  and  $\xi(i, j)$  are deployed as fog aware statistical features.

The contrast energy (*CE*) predicts perceived local contrast on natural images [28]. Although there are many simple measures of contrast including Michelson contrast [39] and the Weber fraction, the perceptual relevance of *CE* [40] supports its choice as a fog aware feature. Each foggy image *I* is decomposed using a bank of Gaussian second-order derivative filters that resemble models of the receptive fields in cortical neurons [41], spanning multiple octaves in spatial scale. All of the filter responses were rectified and divisively normalized to account for the process of non-linear contrast gain control in visual cortex [42]. We could also have used a Gabor receptive field model [43]. These responses are then thresholded to exclude noise [28]. The *CE* is computed separately on the individual color components (grayscale, yellow-blue (*yb*), and red-green (*rg*)) as follows,

$$CE(I_c) = \frac{\alpha \cdot Z(I_c)}{Z(I_c) + \alpha \cdot \kappa} - \tau_c, \quad (11)$$

$$Z(I_c) = \sqrt{(I_c \otimes h_h)^2 + (I_c \otimes h_v)^2}, \quad (12)$$

where  $c \in \{\text{gray}, \text{yb}, \text{rg}\}$  indicates the color channels of *I*;  $\text{gray} = 0.299R + 0.587G + 0.114B$  [44],  $\text{yb} = 0.5(R + G) - B$ , and  $\text{rg} = R - G$  [30]. Here  $\alpha$  is the maximum value of  $Z(I_c)$ ,  $\kappa$  is a contrast gain, and  $\tau_c$  is the noise threshold given a color channel. The symbol  $\otimes$  means convolution, while  $h_h$  and  $h_v$  are the horizontal and vertical second-order derivatives of the Gaussian function, respectively. Following [28], the smallest filter with a standard deviation 0.12 degrees of visual angle corresponding to about 3.25 pixels was used, while the size of a filtering window was 20 pixels. The contrast-gain was fixed at 0.1. The noise thresholds were determined on a separate set of images (a selection of 1800 images from the Corel database) and set to half standard deviation of the average contrast present in that dataset for a given scale and gain. Specifically, the noise thresholds were 0.2353, 0.2287, and 0.0528 for the *gray*, *yb*, and *rg* color channels, respectively [28].

Since foggy images tend to contain less detail, we use the image entropy (*IE*) as a fog aware feature as follows:

$$IE(I) = - \sum_{vi} p(h_i) \log[p(h_i)], \quad (13)$$

where  $p(h_i)$  is the probability of the pixel intensity  $h_i$ , which is estimated from the normalized histogram [29].

The dark channel prior (DCP) is based on the observation that at least one color channel contains a significant percentage

TABLE I  
LIST OF FOG AWARE STATISTICAL FEATURES AND  
METHOD OF COMPUTATION

ID	Feature description	Computation
$f_1$	The variance of MSCN coefficients	(6)
$f_2, f_3$	The variance of the vertical product of MSCN coefficients (positive, negative mode)	(9)
$f_4$	The sharpness	(8)
$f_5$	The coefficient of variance of sharpness	(10)
$f_6, f_7, f_8$	The contrast energy (grayscale, yellow-blue, and red-green)	(11)
$f_9$	The image entropy	(13)
$f_{10}$	The dark channel prior in a pixel-wise	(14)
$f_{11}$	The color saturation in <i>HSV</i> color space	(15)
$f_{12}$	The colorfulness	(16)

of pixels whose luminances are low in most non-sky regions on haze-free images [12]. We use a pixel-wise DCP model [23],

$$I_{\text{dark}}(i, j) = \min_{c \in \{R, G, B\}} [I_c(i, j)], \quad (14)$$

where  $c \in \{R, G, B\}$  represents the *RGB* channels. The range of  $I_{\text{dark}}$  is set to the interval [0, 1]. Regions of high value in  $I_{\text{dark}}$  generally denote sky, fog, or white object regions. Conversely, regions of low value of  $I_{\text{dark}}$  represent fog-free regions.

To measure the visibility of a foggy scene as it is affected by color, we use color saturation and colorfulness as fog aware features. In colorimetry, colorfulness is the degree of difference between a color and gray, while saturation is the colorfulness of a color relative to its own brightness [45]. Since airlight scattered in a foggy atmosphere can cause scene color shifts, color saturation and colorfulness decrease as fog density increases. The color saturation  $I_{\text{saturation}}$  is computed using the saturation channel after transforming an image into *HSV* color space (e.g., by using MATLAB function “*rgb2hsv*”), while colorfulness (*CF*) is computed following [30] as follows,

$$I_{\text{saturation}}(i, j) = I_{\text{HSV}}(i, j, 2), \quad (15)$$

$$CF = \sqrt{\sigma_{rg}^2 + \sigma_{yb}^2} + 0.3 \sqrt{\mu_{rg}^2 + \mu_{yb}^2}, \quad (16)$$

where  $I_{\text{HSV}}$  is a transformed version of *I* into *HSV* color space,  $\sigma_a^2 = \frac{1}{X} \sum_{x=1}^X (a_x^2 - \mu_a^2)$ ,  $\mu_a = \frac{1}{X} \sum_{x=1}^X a_x$ ,  $rg = R - G$ , and  $yb = 0.5(R + G) - B$  [30], and the range of pixel values is  $x = 1 \dots X$ .

All of the features described here are listed in Table I.

### B. Patch Selection

A total of 12 local fog aware features ( $f_1 \dots f_{12}$  described in Table I) are computed from each  $P \times P$  partitioned image patch. To obtain one value per patch for each fog aware statistical feature, we use the average values of each feature  $f_4, f_5, f_6, f_7, f_8, f_{10}$ , and  $f_{11}$  over each patch. For  $f_1, f_2, f_3, f_9$ , and  $f_{12}$ , one value is directly calculated on each image patch. Given a collection of fog aware features from a corpus of 500 foggy images and a corpus of 500 fog-free images, respectively, only a subset of the patches are used. Since every image is subject to some kind of limiting distortions including defocus blur [46], and since humans tend to evaluate the



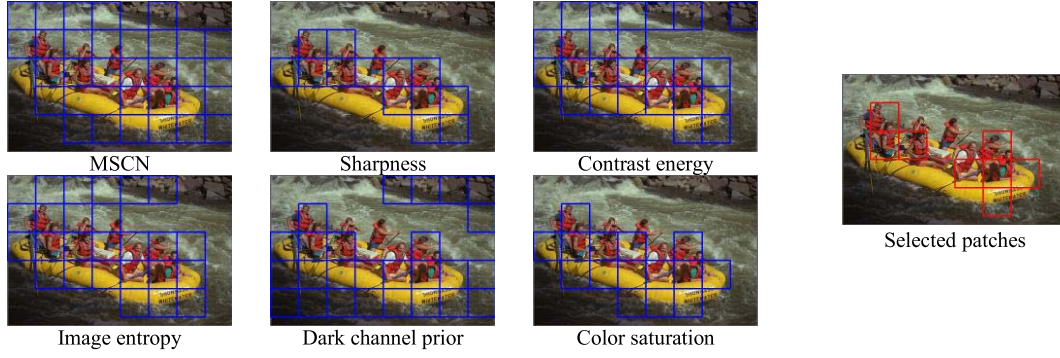


Fig. 2. A patch selection procedure using local fog aware statistical features. The blue patches in the first three columns show patches selected using the feature selection criterion. The red patches in the fourth column denote the selected patches. The patch size is  $96 \times 96$  pixels, while the image size is  $512 \times 768$  pixels.

visibility of foggy images based on regions of high sharpness and contrast, the subset of the image patches drawn from the corpus of foggy and fog-free images are reduced, whereas all patches are used for test foggy images.

The representative image patches that are automatically selected are intended to maximize the amount of information contained in the fog aware features. Let the  $P \times P$  sized patches be indexed  $b = 1, 2, \dots, B$ . For each feature  $f_m(i, j)$ , which denotes feature coefficients at feature number  $m$ , we first compute

$$f_{m,\max}(i, j) = \max_{(i,j) \in 1, \dots, B} [f_m(i, j)], \quad (17-1)$$

$$f_{m,\min}(i, j) = \min_{(i,j) \in 1, \dots, B} [f_m(i, j)], \quad (17-2)$$

on the corpus of fog-free images, then normalize:

$$\hat{f}_m(i, j) = [f_m(i, j) - f_{m,\min}] / (f_{m,\max} - f_{m,\min}). \quad (17-3)$$

For features that are computed on patches (i.e.,  $f_1, f_2, f_3, f_9$ , and  $f_{12}$ ),  $\hat{f}_m(i, j)$  is used for patch selection. For features that are computed in at pixels (i.e.,  $f_4, f_5, f_6, f_7, f_8, f_{10}$ , and  $f_{11}$ ), we executed the process (17) again using the average value of  $\hat{f}_m(i, j)$  for each patch indexed  $b$  at feature  $m$ . In this way, all the  $\hat{f}_m(i, j)$  values satisfy  $0 \leq \hat{f}_m(i, j) \leq 1$ . For  $m = 10$ , we used  $1 - \hat{f}_m(i, j)$ . Then to obtain patches from a corpus of natural fog-free images, we selected the patches satisfying  $\hat{f}_m(i, j) > \text{mean} [\hat{f}_m(i, j)]$  at feature  $m = 1, 4, 6, 9, 10$  and  $11$ . Similarly, to obtain patches from a corpus of natural foggy images, we executed the same process with the opposite inequality. An example of patch selection is shown in Fig. 2. Patch selection was tested over a wide range of patch sizes ranging from  $4 \times 4$  to  $160 \times 160$  pixels. The patch overlap may be varied: generally the performance of the perceptual fog density predictor rises with greater overlap.

### C. Natural Fog-Free and Foggy Image Data Sets

To extract fog aware statistical features from a corpus of fog-free images, we selected 500 natural fog-free images from the LIVE IQA database [47], the Berkeley image segmentation database [48], the IRCCyN/IVC database [49], and the CSIQ database [50]. These diverse images contain a wide variety of natural image content, including landscapes, forests,

buildings, roads, and cities with and without animals, people, and objects. Image sizes vary from  $480 \times 320$  to  $770 \times 512$  pixels.

Similarly, to extract fog aware statistical features from a corpus of foggy images, we selected 500 natural foggy images from copy-right free web sources (e.g., Flickr [51]), a number of foggy images captured by the authors, and well-known test foggy images [8], [10]–[17]. These images contain fog density levels ranging from slightly to heavily dense fog as well as diverse image contents. The image sizes vary from  $300 \times 300$  to  $1128 \times 752$  pixels. The foggy and fog-free images that were used in our experiments can be found at <http://live.ece.utexas.edu/research/fog/index.html>.

### D. Prediction of Perceptual Fog Density

A test foggy image is partitioned into  $P \times P$  patches. All patches are then used to compute the average feature values, thereby yielding a set of 12 fog aware statistical features for each patch. Next, the foggy level  $D_f$  of the test foggy image is predicted using a Mahalanobis-like distance measure between a MVG fit to the fog aware statistical features extracted from the test foggy image and a nominal MVG model of fog aware features extracted from the corpus of 500 natural fog-free images. The MVG probability density in  $d$  dimensions is

$$\text{MVG}(\mathbf{f}) = \frac{1}{(2\pi)^{d/2} |\Sigma|^{1/2}} \exp \left[ -\frac{1}{2} (\mathbf{f} - \mathbf{v})^t \Sigma^{-1} (\mathbf{f} - \mathbf{v}) \right], \quad (18)$$

where  $\mathbf{f}$  is the set of fog aware statistical features described in Table I,  $\mathbf{v}$  and  $\Sigma$  denote the mean and  $d$ -by- $d$  covariance matrix, and  $|\Sigma|$  and  $\Sigma^{-1}$  are the determinant and inverse of the covariance matrix of the MVG model density, respectively. The mean and covariance matrix are estimated using a standard maximum likelihood estimation procedure following [31].

Prior to feeding the fog aware features into the MVG fit or model, the fog aware features are subjected to a logarithmic nonlinearity. Next, a Mahalanobis-like distance measure,

$$D_f(\mathbf{v}_1, \mathbf{v}_2, \Sigma_1, \Sigma_2) = \sqrt{(\mathbf{v}_1 - \mathbf{v}_2)^t \left( \frac{\Sigma_1 + \Sigma_2}{2} \right)^{-1} (\mathbf{v}_1 - \mathbf{v}_2)}, \quad (19)$$

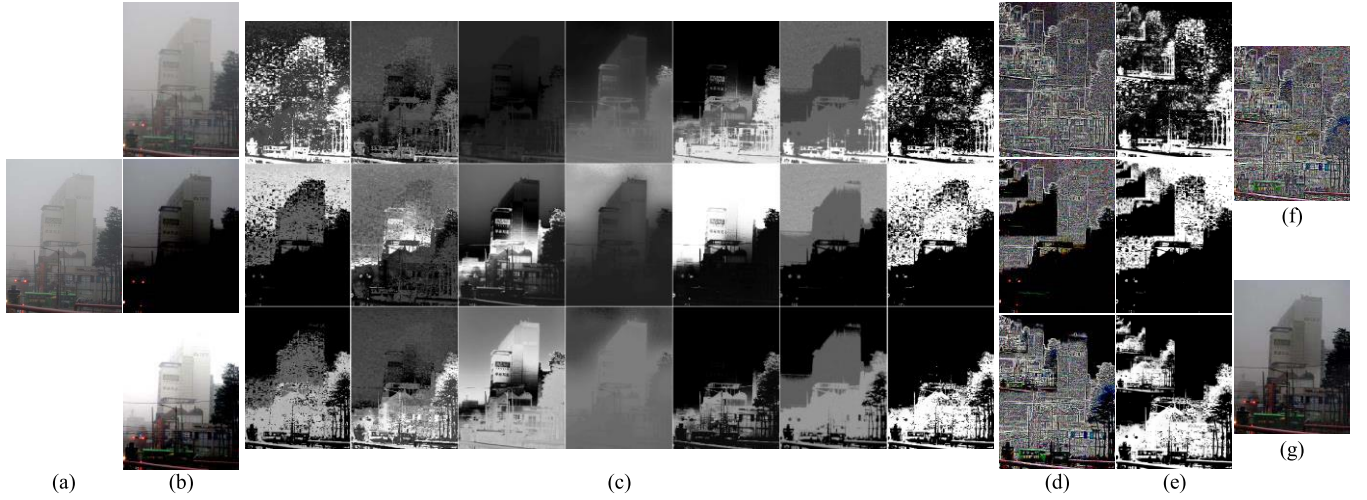


Fig. 3. Overall sequence of processes comprising DEFADE on example images. (a) Input foggy image  $I$ . (b) Preprocessed images: white balanced image  $I_1$ , contrast enhanced image after mean subtraction  $I_2$ , and fog aware contrast enhanced image  $I_3$ , from top to bottom. (c) Weight maps: the first, second, and third rows are weight maps on preprocessed images  $I_1$ ,  $I_2$ , and  $I_3$ , respectively. Chrominance, saturation, saliency, perceptual fog density, luminance, contrast, and normalized weight maps are shown from left to right column. (d) Laplacian pyramids of the preprocessed images  $I_1$ ,  $I_2$ , and  $I_3$ , from top to bottom. (e) Gaussian pyramids of the normalized weight maps corresponding to  $I_1$ ,  $I_2$ , and  $I_3$ , from top to bottom. (f) Multi-scale fused pyramid  $F_l$ , where  $l = 9$ . (g) Output defogged image.

where  $\mathbf{v}_1$ ,  $\mathbf{v}_2$  and  $\Sigma_1$ ,  $\Sigma_2$  are the mean vectors and covariance matrices of the MVG model of the fog-free corpus and the MVG fit of the test image, respectively. Similarly, the fog-free level  $D_{ff}$  of a test foggy image is also predicted as a distance between the MVG fit to the fog aware statistical features extracted from the test foggy image and a nominal MVG model from a corpus of 500 natural foggy images.

Finally, the perceptual fog density  $D$  of a given foggy image to be evaluated is achieved as follows,

$$D = \frac{D_f}{D_{ff} + 1}, \quad (20)$$

where a stabilization constant “1” is used to prevent the denominator from becoming too small. Smaller values of  $D$  indicate lower perceptual fog density.

#### IV. PERCEPTUAL IMAGE DEFOGGING

We propose a powerful and useful direct application of FADE: perceptual image defogging, dubbed *DEnsity of Fog Assessment-based Defogger* (DEFADE). DEFADE utilizes statistical regularities observed in foggy and fog-free images to extract visible information from three preprocessed images: one white balanced and two contrast enhanced images. Chrominance, saturation, saliency, perceptual fog density, fog aware luminance, and contrast weight maps are applied on the preprocessed images using Laplacian multiscale refinement. The overall processes of DEFADE are shown in Fig. 3 with examples of each stage, as detailed in the following.

##### A. Preprocessing

The first preprocessed image  $I_1$  is white balanced to adjust the natural rendition of the output by eliminating chromatic casts caused by atmospheric color. The shades-of-gray color constancy technique [52] is used because it was fast and robust.

The second and the third preprocessed images are contrast enhanced images. Ancuti and Ancuti [17] derived a contrast enhanced image by subtracting the average luminance value,  $\bar{I}$ , of the image  $I$  from the foggy image  $I$ , then applying a multiplicative gain. Thus  $I_2 = \gamma(I - \bar{I})$ , where  $\gamma = 2.5$  [17]. Although  $\bar{I}$  is a good estimate of image brightness, problems can arise in very dark image regions or on denser foggy images. Regions of positive  $(I - \bar{I})$  typically indicate rough foggy regions, hence the contrasts of these areas can be ostensibly improved by a multiplicative gain. However, severe dark aspects, where negative values of  $(I - \bar{I})$  occur, may dominate as  $\bar{I}$  increases, as shown on  $I_2$  in Fig. 3(b). When  $\bar{I}$  is too small,  $I_2$  can saturate causing severe white aspects. Therefore, finding an appropriate value is important.

To overcome these limitations, we create another type of preprocessed image using FADE,

$$I_3 = \gamma[I - \mu(I_{\text{least\_foggy}})], \quad (21)$$

where  $\mu(I_{\text{least\_foggy}})$  is the average luminance of only the least foggy regions of  $I$ . To compensate for severe dark aspects caused by  $I_2$  (especially on dense foggy regions),  $\mu(I_{\text{least\_foggy}})$  is preferred to significantly differ from  $\bar{I}$  to include wide-range exposure inputs during the multiscale refinement, yielding high contrast and detailed edges [19]. The perceptual fog density map predicted by FADE on  $I$  using overlapped  $8 \times 8$  patches is filtered by a guided filter [13] to reduce noise, and then is scaled to  $[0, 1]$  by dividing the predicted fog density range by its maximum value. Let the denoised and scaled fog density map be  $D_{\text{map\_N}}$ . The least foggy regions are defined as

$$\hat{I}_{\text{least\_foggy}}(i, j) = \arg \max_{(i, j)} [\bar{I} - \mu\{I_{\text{least\_foggy}}(i, j)\}], \quad (22)$$

where  $\hat{I}_{\text{least\_foggy}}(i, j)$  is estimated by searching areas satisfying  $D_{\text{map\_N}} \leq 0.01 \cdot k$ , where  $k$  is an integer

index ( $0 \leq k \leq 50$ ). The regions where  $D_{\text{map}_N} = 0$  are fog-free regions, while the regions where  $D_{\text{map}_N} = 0.5$  are presumed to be moderate fog-density areas. Since  $\hat{I}_{\text{least\_foggy}}(i, j)$  dynamically adjusts the contrast of  $I_3$  based on  $\bar{I}$  and  $D_{\text{map}_N}$ , a new preprocessed image  $I_3$  effectively removes the severe dark aspects of  $I_2$  during the multiscale refinement and enhances the visibility of the defogged image. An input foggy image and its corresponding preprocessed images are shown in Figs. 3(a) and 3(b), respectively.

### B. Weight Maps

The weight maps selectively weight the most visible regions of the preprocessed images. In [17], three weight maps were defined based on measurements of chrominance, saturation, and saliency. We used this set of objective weight maps, and further propose the use of a new set of perceptually-motivated fog aware weight maps. The fog aware weight maps accurately capture the perceptual visibility of the preprocessed images, thereby producing more detailed edges and vivid color on the visibility enhanced images.

The **chrominance weight map**  $W_{chr}$  measures the loss of colorfulness by taking higher values at colorful pixels that are assumed to be a part of fog-free regions. The **saturation weight map**  $W_{sat}$  controls the saturation gain between local saturation  $S$  and the maximum saturation ( $S_{\text{max}} = 1$ ) in *HSV* color space. The **saliency weight map**  $W_{sal}$  shows the degree of local conspicuity, by highlighting potentially salient regions by enhancing the local contrast. These maps are computed as follows:

$$W_{chr}^k = \sqrt{1/3[(R^k - I_{gray}^k)^2 + (G^k - I_{gray}^k)^2 + (B^k - I_{gray}^k)^2]}, \quad (23)$$

$$W_{sat}^k = \exp\left(-(S^k - S_{\text{max}})^2/2\sigma^2\right), \quad (24)$$

$$W_{sal}^k = \|I_k^{w_{hc}} - I_k^\mu\|, \quad (25)$$

where  $k$  is an index on the preprocessed images, and where  $R^k$ ,  $G^k$ ,  $B^k$ , and  $I_{gray}^k$  are the red, green, blue color channels and the grayscale channel of  $I_k$ . The standard deviation  $\sigma = 0.3$  [17].  $I_k^{w_{hc}}$  is a Gaussian smoothed version of  $I_k$ ,  $I_k^\mu$  is the mean of  $I_k$  in *Lab* color space, and  $\|\cdot\|$  is the  $L_2$  norm [53].

The **fog density weight map** guides the other weight maps to accurately balance fog-free and foggy regions. A perceptual fog density map on  $I$  is predicted using FADE on overlapped  $8 \times 8$  patches, then a guided filter [13] is applied to reduce noise. The range of the denoised fog density map is scaled to  $[0, 1]$ . As can be seen in Fig. 3(b), since  $I_2$  captures significant information regarding denser foggy regions of  $I$ , the denoised and scaled fog density map  $D_{\text{map}_N}$  serves as the fog density weight map of  $I_2$ , and the other fog density maps are decided as follows:

$$\begin{aligned} W_{fog}^1 &= 1 - D_{\text{map}_N}, & W_{fog}^2 &= D_{\text{map}_N}, \\ W_{fog}^3 &= W_{fog}^1 \times W_{fog}^2, \end{aligned} \quad (26)$$

where  $W_{fog}^3$  is also scaled to  $[0, 1]$ .

The **fog aware luminance weight map** represents how close the luminances of the preprocessed images are to the

luminance of the least foggy areas of  $I$ . Since contrast enhancement often causes a shift in the luminance profiles of the processed images [54], yielding dark patches or a faded appearance, the fog aware luminance weight map seeks to alleviate these degradations by allocating a high value to luminances closer to  $\mu(I_{\text{least\_foggy}})$ . The map is created using a Gaussian weighting function for each *RGB* color channel, which are multiplied as follows,

$$W_{lum}^k = W_{lum\_R}^k \times W_{lum\_G}^k \times W_{lum\_B}^k, \quad (27)$$

$$W_{lum\_i}^k = \exp\left(-[I_k^i - \mu(I_{\text{least\_foggy}}^i)]^2/2\sigma^2\right), \quad (28)$$

where  $I_k^i$  is the color channel of  $I_k$ , and  $\mu(I_{\text{least\_foggy}}^i)$  is the mean luminance of  $I_{\text{least\_foggy}}^i$  at  $i \in \{R, G, B\}$ , and where  $\sigma = 0.2$  [54].

The **contrast weight map** improves image details by assigning higher weights at regions of high gradient values. The map is expressed as a local weighted contrast:

$$\begin{aligned} W_{con}^k(i, j) &= \sqrt{\sum_{p=-P}^P \sum_{q=-Q}^Q \omega_{p,q} [I_{gray}^k(i+p, j+q) - \mu_k(i, j)]^2}, \end{aligned} \quad (29)$$

$$\begin{aligned} \mu_k(i, j) &= \sum_{p=-P}^P \sum_{q=-Q}^Q \omega_{p,q} I_{gray}^k(i+p, j+q), \end{aligned} \quad (30)$$

where  $i \in \{1, 2, \dots, M\}$ ,  $j \in \{1, 2, \dots, N\}$  are spatial indices,  $M$  and  $N$  are image dimensions.  $\omega = \{\omega_{p,q} | p = -P, \dots, P, q = -Q, \dots, Q\}$  is a 2D circularly symmetric Gaussian weighting function sampled out to 3 standard deviations ( $P = Q = 3$ ) and rescaled to unit volume [27], and  $I_{gray}^k$  is the grayscale version of  $I_k$ .

Normalized weight maps are obtained to ensure that they sum to unity as follows:

$$\bar{W}^k = W^k / \sum_k W^k, \quad (31)$$

where  $W^k = W_{chr}^k W_{sat}^k W_{sal}^k W_{fog}^k W_{lum}^k W_{con}^k$ , and  $k$  is the index of  $I_k$ . Figure 3(c) shows examples of weight maps.

### C. Multiscale Refinement

Multiscale refinement is used to prevent halo artifacts which can occur near strong transitions within the weight maps [17]. The multiscale approach is motivated by the fact that the human visual system is sensitive to local changes (e.g., edges) over a wide range of scales, and that the multiscale method provides a convenient way to incorporate local image details over varying resolutions [19], [54]. Each preprocessed image and the corresponding normalized weight map are decomposed using a Laplacian pyramid and a Gaussian pyramid [55], respectively, then they are blended to yield a fused pyramid

$$F_l = \sum_k G_l\{\bar{W}^k\} L_l\{I_k\}, \quad (32)$$

where  $l$  is the number of pyramid levels. In our experiment,  $l = 9$  to eliminate fusion degradation.  $G_l\{\cdot\}$  and  $L_l\{\cdot\}$  represent the Gaussian and the Laplacian decomposition at pyramid level  $l$ , respectively. Operations are performed successively on each level, in a bottom-up manner. Finally, a defogged





Fig. 4. Example images from the 100 test images used in the human study.

image  $J$  is achieved by Laplacian pyramid reconstruction as follows,

$$J = \sum_l F_l \uparrow^n, \quad (33)$$

where  $\uparrow^n$  is an upsampling operator with factor  $n = 2^{l-1}$  [17]. Figures 3(d) - 3(g) show the Laplacian, the Gaussian, the fused pyramid, and the defogged image, respectively.

## V. TEST SETUP

Since previous visibility prediction models require reference fog-free, multiple foggy, diverse polarization images, or side geographical information obtained using an onboard camera, it is not possible to directly compare the performance of FADE with other prediction models. Instead, we evaluated the performance of FADE against the results of a human subjective study. To objectively evaluate the performance of DEFADe, we used the contrast enhancement assessment method of Hautière *et al.* [22] and the perceptual fog density  $D$  of FADE.

### A. Human Subjective Study

1) *Test Images*: One hundred color images were selected to capture adequate diversity of image content and fog density from newly recorded foggy images, well-known foggy test images (none contained in the corpus of 500 foggy images in Section III-C) [8], [10]–[17], and corresponding defogged images. Some images were captured by a surveillance camera, while others were recorded on the same scene under a variety of fog density conditions. The image sizes varied from  $425 \times 274$  to  $1024 \times 768$  pixels. Some sample images are shown in Fig. 4.

#### 2) Test Methodology:

a) *Subjects*: A total of 20 naïve students at The University of Texas at Austin attended the subjective study. All subjects were between the ages of 20 and 35. No vision test was performed although a verbal confirmation of soundness of (corrected) vision was obtained from the subjects. The study was voluntary and no monetary compensation was provided to the subjects.

b) *Equipment and display configuration*: We developed the user interface for the study on a Windows PC using MATLAB and the Psychophysics toolbox [56], which interfaced with a NVIDIA GeForce GT640M graphics card in an Intel® Core™ i7-3612QM CPU @2.10GHz processor, with 8GB RAM. The screen was set at a resolution of



Fig. 5. Screenshot of the subjective study interface: (a) displaying the image and (b) rating bar to judge fog density.

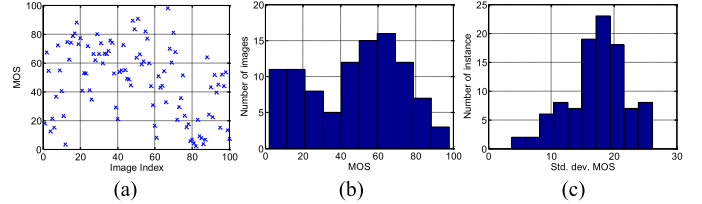


Fig. 6. (a) MOS of 100 test images. (b) Associated histogram of MOS scores. (c) MOS standard deviation histogram.

$1920 \times 1080$  pixels at 60Hz, while the test images were displayed at the center of the 15" LCD monitor (Dell, Round Rock, TX, USA) for 8 seconds at their native image resolution to prevent any distortions due to scaling operations performed by software or hardware. No errors such as latencies were encountered while displaying the images. The remaining areas of the display were black as shown in Fig. 5(a). Subjects viewed the monitor from an approximate viewing distance of about 2.25 screen heights.

c) *Design and procedure*: We adopted a single-stimulus continuous quality evaluation (SSCQE) [57] procedure. The subjects were requested to rate the fog density of the test images at the end of each display. A continuous slider bar with Likert-like markings “Hardly,” “Little,” “Medium,” “Highly,” and “Extremely” to indicate the degree of perceived fog density, was displayed on the center of the screen, where, for example, “Highly” corresponded to “I think the test image is highly foggy.” The recorded subjective judgments were converted into fog density scores by linearly mapping the entire scale to the integer interval  $[0, 100]$ , where 0 would indicate almost fog-free. Figure 5 shows the subjective study interface. Each subject attended one session that lasted no more than 30 minutes. A short training set using ten diverse foggy images different from the test images preceded the actual study to familiarize the subject with the procedure. No demand was made of the subjects to compel them to utilize the entire scale when rating the images since we believe such a procedure leads to less natural and possibly biased judgments.

3) *Processing of the Subjective Scores*: Since no subject was rejected in the data screening procedure [57], all study data were used to form a Mean Opinion Scores (MOS) for each image. Specifically, let  $s_{ij}$  denote the score assigned by subject  $i$  to the test image  $j$  and  $N_j$  be the total number of rating received for test image  $j$ . The MOS is then

$$MOS_j = \frac{1}{N_j} \sum_i s_{ij}. \quad (34)$$

Figure 6 plots MOS across 100 test images as well as the corresponding histograms of MOS and MOS standard

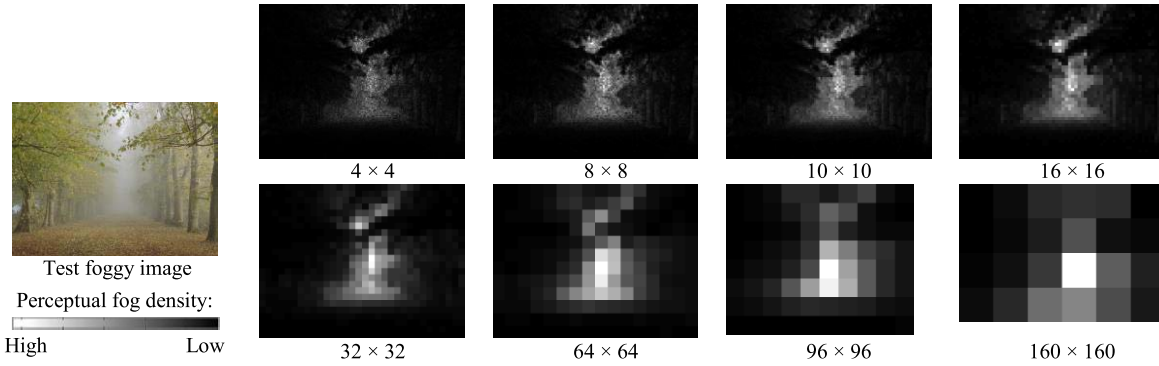


Fig. 7. Results of the proposed perceptual fog density prediction model FADE over patch sizes ranging from  $4 \times 4$  to  $160 \times 160$  pixels. The predicted perceptual fog density is indicated by gray levels ranging from black (low density) to white (high density).

deviation, clearly demonstrating that the test images effectively span the entire perceptual range of fog densities.

### B. Quantitative Evaluation Methods

1) *Full-Reference Contrast Enhancement Assessment*: The measure of Hautière *et al.* [22] provides a quantitative evaluation of a defogging algorithm using three metrics which are based on the ratio between the gradients of the foggy image and the corresponding defogged image. The metric  $e$  represents the rate of new visible edges in the defogged image against the foggy image, while the metric  $\Sigma$  denotes the percentage of pixels that become black or white following defogging. A higher positive value of  $e$  and a value of  $\Sigma$  closer to zero imply better performance. The metric  $\bar{r}$  denotes the mean ratio of the gradient norms before and after defogging. A higher value of  $\bar{r}$  represents stronger restoration of the local contrast, whereas low values of  $\bar{r}$  suggest fewer spurious edges and artifacts.

2) *No-Reference Perceptual Fog Density Assessment*: The perceptual fog density  $D$  delivered by FADE is a no-reference method that does not require the original foggy image. A lower value of  $D$  implies better defogging performance.

## VI. RESULTS AND PERFORMANCE EVALUATION

### A. Results of FADE

The proposed model FADE not only predicts perceptual fog density of an entire image, but also provides a local perceptual fog density prediction on each patch. The patch size can vary and can be overlapped depending on whether an application requires different density measurements. Figure 7 demonstrates the results of applying FADE using non-overlapped patch sizes ranging from  $4 \times 4$  to  $160 \times 160$  pixels, where the predicted fog density is shown visually in gray scales ranging from black (low density) to white (high density). Using a smaller patch size yields more detailed fog density maps. More results of perceptual fog density prediction using FADE can be found at <http://live.ece.utexas.edu/research/fog/index.html>.

### B. Evaluation of FADE Performance

We utilized Pearson's linear correlation coefficient (LCC) and Spearman's rank ordered correlation coefficient (SROCC)

TABLE II  
LCC AND SROCC BETWEEN ALGORITHM SCORES AND THE MOS OVER DIFFERENT PATCH SIZES

Patch size	$4 \times 4$	$8 \times 8$	$10 \times 10$	$16 \times 16$	$32 \times 32$	$64 \times 64$	$96 \times 96$	$160 \times 160$
LCC	0.8896	0.8899	0.8922	<b>0.8934</b>	0.8835	0.8614	0.8560	0.8331
SROCC	0.8720	<b>0.8756</b>	0.8742	0.8723	0.8647	0.8459	0.8361	0.8038

between the algorithm scores of FADE and MOS recorded from human subjects on the 100 test images. The predicted perceptual fog density scores of FADE were passed through a logistic non-linearity [47] before computing LCC relative to subjective fog density scores.

Table II tabulates the performance of FADE in terms of LCC and SROCC for diverse patch sizes ranging from  $4 \times 4$  to  $160 \times 160$  pixels on the 100 test images. The results indicate that the best performing patch size for predicting perceptual fog density using FADE was  $8 \times 8$  pixels for LCC and  $16 \times 16$  pixels for SROCC, where the LCC after nonlinear regression and SROCC were 0.8934 and 0.8756, respectively. However, Table II also strongly suggests that the LCC and SROCC values are quite stable over a wide range of patch sizes. When the patch size increased beyond  $32 \times 32$  pixels, performance decreased a little, probably from a loss of locality of capturing detail.

Figure 8 shows predicted perceptual fog densities  $D$  delivered by FADE using an  $8 \times 8$  patch size and judged fog densities by human subjects on the 100 test images. Lower  $D$  and MOS scores denote less fog. Representative images shown in the corners of Fig. 8 demonstrate that  $D$  values are strongly indicative of perceived fog densities.

As an application, we also tested how FADE can be used to evaluate the performance of defogging algorithms. Although metrics for assessing the results of defogging methods against pristine (fog-free) reference images are available [22], [58], metrics for NR assessment of defogging algorithms have not been reported. We validate the possibility of FADE as a NR assessment tool for evaluating defogging algorithms by comparing the predicted perceptual fog density of defogged images against the perceived fog density from human subjects. Figure 9 shows two sets of test images used in the validation process, which include two foggy images and the corresponding eight defogged images yielded from diverse

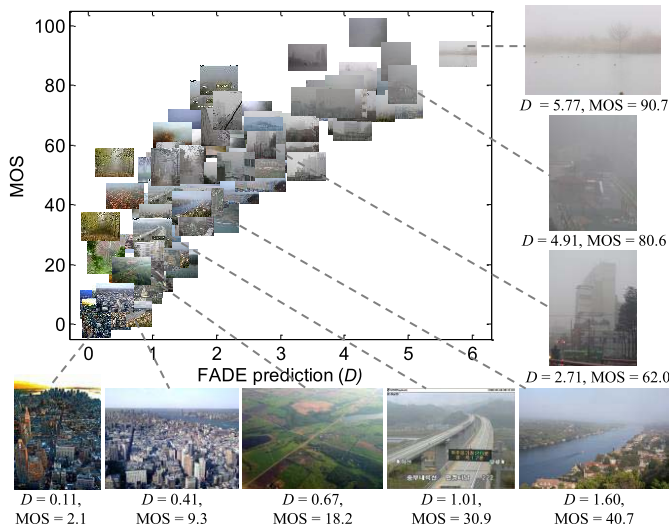


Fig. 8. Predicted perceptual fog densities delivered by FADE using an  $8 \times 8$  patch and judged fog densities by human subjects for the 100 test images.

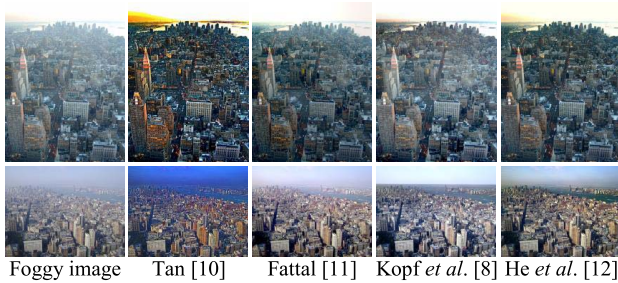


Fig. 9. Foggy and corresponding defogged images used in the human study.

TABLE III

LCC AND SROCC BETWEEN ALGORITHM SCORES AND THE MOS ON 10 TEST IMAGES SHOWN IN FIG. 9

Patch size	$4 \times 4$	$8 \times 8$	$10 \times 10$	$16 \times 16$	$32 \times 32$	$64 \times 64$	$96 \times 96$	$160 \times 160$
LCC	0.9416	0.9406	0.9403	0.9400	0.9389	0.9377	0.9348	<b>0.9697</b>
SROCC	0.6121	0.6121	0.6727	0.7212	0.6727	0.6606	0.6121	<b>0.7576</b>

defogging methods [8], [10]–[12]. As shown in Table III, the high LCC and SROCC values between the predicted perceptual fog densities delivered by FADE and the judged fog densities reported by the human subjects indicate that FADE can be a useful tool to evaluate the performance of defogging algorithms. Although the use of  $160 \times 160$  patch sizes delivered the best numerical performance, large patch sizes reveal significant less detail.

### C. Evaluation of DEFADe Performance

A large number of foggy images were tested to evaluate the performance of DEFADe. First, we compared the defogged images obtained using the method of Ancuti and Ancuti [17] and ours on darker, denser foggy images. As shown in Fig. 10, DEFADe achieves better restoration of the contrast of edges and of vivid colors. We also executed a quantitative evaluation of defogged outputs using the contrast enhancement measure of Hautière *et al.* [22] and the perceptual fog density  $D$

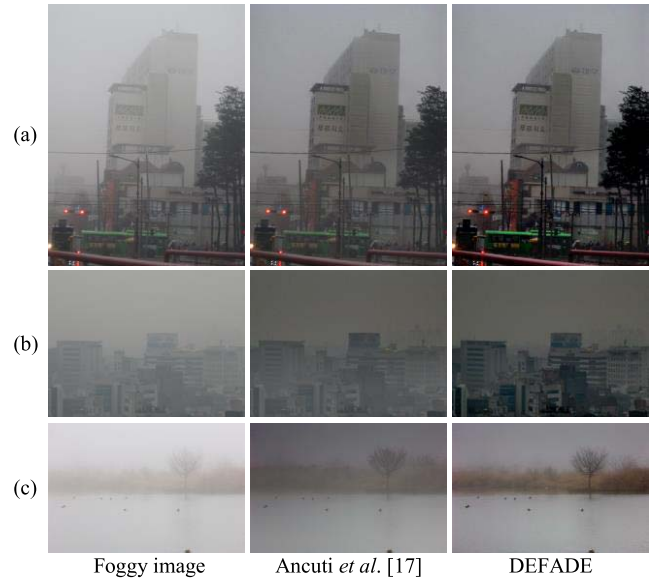


Fig. 10. Defogged images using Ancuti *et al.*'s method [17] and DEFADe.

TABLE IV

QUANTITATIVE COMPARISON OF DEFOGGED IMAGES SHOWN IN FIG. 10 USING  $e$ ,  $\Sigma$ ,  $\bar{r}$  OF ANCUTI *et al.* [23] AND  $D$  DESCRIBED IN SECTION III

Foggy image	Ancuti <i>et al.</i> [17]				DEFADe			
	$D$	$e$	$\Sigma$	$\bar{r}$	$D$	$e$	$\Sigma$	$\bar{r}$
(a)	2.71	0.28	0.00	1.12	1.64	0.77	0.02	1.66
(b)	3.46	7.40	0.00	1.89	1.73	30.20	0.00	2.38
(c)	5.77	13.08	0.00	1.50	2.64	63.59	0.00	2.35

described in Section V-B. As can be seen in Table IV, high values of the metric  $e$  and low values of the metric  $\Sigma$  show that DEFADe produces more naturalistic, clear edges and rich colors after defogging while maintaining a lower percentage of saturated black or white pixels. The low values of the metric  $D$  denote that foggy images are more effectively and perceptually defogged by DEFADe.

Next, we compared the defogged images obtained using the models of Tan [10], Fattal [11], Kopf [8], He *et al.* [12], Tarel and Hautière [14], Ancuti and Ancuti [17], and DEFADe on standard test foggy images. From Fig. 11, it can be seen that the defogged images produced by Tan and Tarel *et al.* look oversaturated and contain halo effects. Fattal's method partially defogged the images near the skylines of the scene, while Tarel *et al.* yields darker sky regions (e.g., ny17). The images defogged by He *et al.*, Ancuti *et al.*, and DEFADe restore more natural colors. Among these the defogged images delivered by DEFADe reveal more sharp details. The quantitative results in Table V also indicate that the methods of He *et al.*, Ancuti *et al.*, and DEFADe restore more visible edges attaining positive values of the metric  $e$ , on which DEFADe significantly reduces the perceptual fog density. Although the method of Tan achieves the greatest reduction of perceptual fog density after restoration, most defogged images produced by that method lose visible edges yielding higher values of the metrics  $\Sigma$  and  $\bar{r}$  due to oversaturation.

Overall, the subjective and objective comparison results in Figs. 10, 11 and Tables IV, V demonstrate that FADE



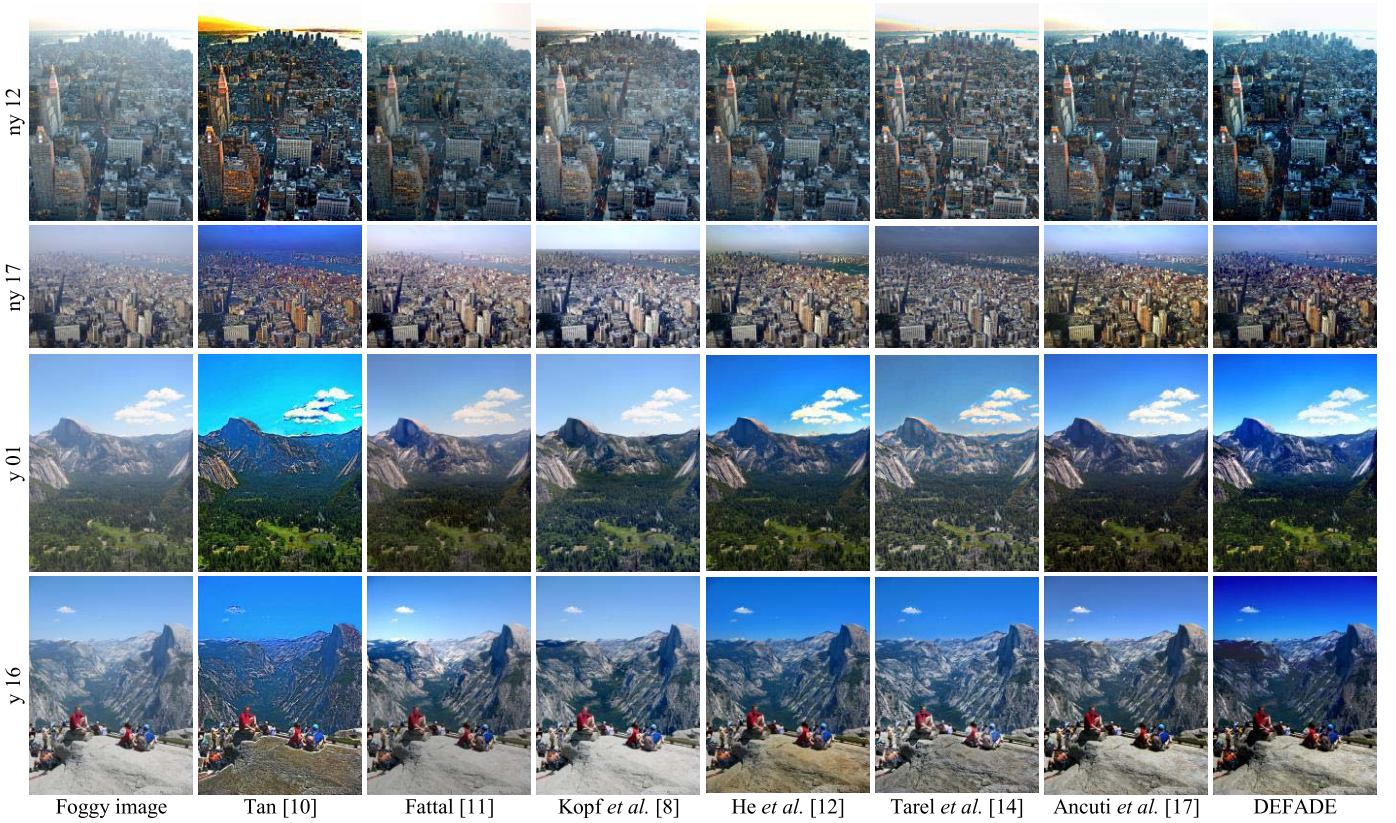


Fig. 11. Comparison of defogged images using Tan [10], Fattal [11], Kopf *et al.* [8], He *et al.* [12], Tarel and Hautière [14], Ancuti and Ancuti [17], and the proposed method.

TABLE V

QUANTITATIVE COMPARISON OF DEFOGGED IMAGES SHOWN IN FIG. 11 USING  $e$ ,  $\Sigma$ ,  $\bar{r}$  OF ANCUTI *et al.* [23] AND  $D$  DESCRIBED IN SECTION III

Foggy image	Tan [10]				Fattal [11]				Kopf <i>et al.</i> [8]				He <i>et al.</i> [12]				Tarel <i>et al.</i> [14]				Ancuti <i>et al.</i> [17]				DEFADE				
	$D$	$e$	$\Sigma$	$\bar{r}$	$D$	$e$	$\Sigma$	$\bar{r}$	$D$	$e$	$\Sigma$	$\bar{r}$	$D$	$e$	$\Sigma$	$\bar{r}$	$D$	$e$	$\Sigma$	$\bar{r}$	$D$	$e$	$\Sigma$	$\bar{r}$	$D$	$e$	$\Sigma$	$\bar{r}$	$D$
ny12	0.73	-0.14	0.02	2.34	0.11	-0.06	0.09	1.32	0.26	0.05	0.00	1.42	0.48	0.06	0.00	1.42	0.42	0.07	0.00	1.88	0.24	0.02	0.00	1.49	0.31	0.09	0.00	1.56	0.20
ny17	0.67	-0.06	0.01	2.22	0.17	-0.12	0.02	1.56	0.36	0.01	0.01	1.62	0.41	0.01	0.00	1.65	0.27	-0.01	0.00	1.87	0.24	0.12	0.00	1.54	0.30	0.03	0.00	1.49	0.20
y01	0.91	0.08	0.01	2.28	0.18	0.04	0.02	1.23	0.51	0.09	0.00	1.62	0.51	0.08	0.01	1.33	0.29	0.02	0.00	2.09	0.31	0.07	0.01	1.19	0.33	0.12	0.00	1.51	0.26
y16	0.63	-0.08	0.01	2.08	0.21	0.03	0.00	1.27	0.43	-0.01	0.00	1.34	0.48	0.06	0.00	1.42	0.27	-0.01	0.00	2.01	0.25	0.18	0.01	1.46	0.33	0.15	0.03	1.44	0.24

achieves better visibility enhancement than state of the art single image defogging algorithms. More defogged results can be found at <http://live.ece.utexas.edu/research/fog/index.html>.

## VII. CONCLUSION

We have described a prediction model of perceptual fog density called FADE and a perceptual image defogging algorithm dubbed DEFADE, both based on image NSS and fog aware statistical features. FADE predicts the degree of visibility of a foggy scene from a single image, while DEFADE enhances the visibility of a foggy image without any reference information such as multiple foggy images of the same scene, different degrees of polarization, salient objects in the foggy scene, auxiliary geographical information, a depth-dependent transmission map, content oriented assumptions, and even without training on human-rated judgments.

FADE utilizes only measurable deviations from statistical regularities observed in natural foggy and fog-free images. We detailed the model and the fog aware statistical features,

and demonstrated how the fog density predictions produced by FADE correlate well with human judgments of fog density taken in a subjective study on a large foggy image database. As an application, we validated that FADE can be a useful, NR tool for evaluating the performance of defogging algorithms. Lastly, we demonstrated that a FADE based, referenceless perceptual image defogging algorithm DEFADE achieves better results on darker, denser foggy images as well as on standard defog test images than state of the art defogging algorithms. Future work could involve developing hardware friendly versions of DEFADE suitable for integrated circuit implementation and the development of mobile image defogging apps.

## REFERENCES

- [1] S. K. Nayar and S. G. Narasimhan, "Vision in bad weather," in *Proc. IEEE Int. Conf. Comput. Vis.*, Sep. 1999, pp. 820–827.
- [2] S. G. Narasimhan and S. K. Nayar, "Contrast restoration of weather degraded images," *IEEE Trans. Pattern Anal. Mach. Intell.*, vol. 25, no. 6, pp. 713–724, Jun. 2003.



- [3] D. Pomerleau, "Visibility estimation from a moving vehicle using the RALPH vision system," in *Proc. IEEE Intell. Transp. Syst.*, Nov. 1997, pp. 906–911.
- [4] Y. Y. Schechner, S. G. Narasimhan, and S. K. Nayar, "Instant dehazing of images using polarization," in *Proc. IEEE Conf. Comput. Vis. Pattern Recognit.*, vol. 1, Dec. 2001, pp. 1–325–I-332.
- [5] N. Hautière, J.-P. Tarel, J. Lavenant, and D. Aubert, "Automatic fog detection and estimation of visibility distance through use of an onboard camera," *Mach. Vis. Appl.*, vol. 17, no. 1, pp. 8–20, Apr. 2006.
- [6] P. S. Chavez, "An improved dark-object subtraction technique for atmospheric scattering correction of multispectral data," *Remote Sens. Environ.*, vol. 24, no. 3, pp. 459–479, 1988.
- [7] N. Hautière, J.-P. Tarel, and D. Aubert, "Towards fog-free in-vehicle vision systems through contrast restoration," in *Proc. IEEE Conf. Comput. Vis. Pattern Recognit.*, Jun. 2007, pp. 1–8.
- [8] J. Kopf et al., "Deep photo: Model-based photograph enhancement and viewing," *ACM Trans. Graph.*, vol. 27, no. 5, 2008, Art. ID 116.
- [9] H. Koschmieder, "Theorie der horizontalen sichtweite: Kontrast und Sichtweite," in *Beiträge zur Physik der freien Atmosphäre*, vol. 12. Munich, Germany: Keim & Nennich, 1924, pp. 171–181.
- [10] R. T. Tan, "Visibility in bad weather from a single image," in *Proc. IEEE Conf. Comput. Vis. Pattern Recognit.*, Jun. 2008, pp. 1–8.
- [11] R. Fattal, "Single image dehazing," *ACM Trans. Graph.*, vol. 27, no. 3, 2008, Art. ID 72.
- [12] K. He, J. Sun, and X. Tang, "Single image haze removal using dark channel prior," in *Proc. IEEE Conf. Comput. Vis. Pattern Recognit.*, Jun. 2009, pp. 1956–1963.
- [13] K. He, J. Sun, and X. Tang, "Guided image filtering," *IEEE Trans. Pattern Anal. Mach. Intell.*, vol. 35, no. 6, pp. 1397–1409, Jun. 2013.
- [14] J.-P. Tarel and N. Hautière, "Fast visibility restoration from a single color or gray level image," in *Proc. IEEE Int. Conf. Comput. Vis.*, Sep./Oct. 2009, pp. 2201–2208.
- [15] L. Kratz and K. Nishino, "Factorizing scene albedo and depth from a single foggy image," in *Proc. IEEE Int. Conf. Comput. Vis.*, Sep./Oct. 2009, pp. 1701–1708.
- [16] K. Nishino, L. Kratz, and S. Lombardi, "Bayesian defogging," *Int. J. Comput. Vis.*, vol. 98, no. 3, pp. 263–278, 2012.
- [17] C. O. Ancuti and C. Ancuti, "Single image dehazing by multi-scale fusion," *IEEE Trans. Image Process.*, vol. 22, no. 8, pp. 3271–3282, Aug. 2013.
- [18] H. B. Mitchell, *Image Fusion: Theories, Techniques and Applications*. New York, NY, USA: Springer-Verlag, 2010.
- [19] T. Mertens, J. Kautz, and F. Van Reeth, "Exposure fusion: A simple and practical alternative to high dynamic range photography," *Comput. Graph. Forum*, vol. 28, no. 1, pp. 161–171, 2009.
- [20] K. B. Gibson and T. Q. Nguyen, "A no-reference perceptual based contrast enhancement metric for ocean scenes in fog," *IEEE Trans. Image Process.*, vol. 22, no. 10, pp. 3982–3993, Oct. 2013.
- [21] A. C. Bovik, "Automatic prediction of perceptual image and video quality," *Proc. IEEE*, vol. 101, no. 9, pp. 2008–2024, Sep. 2013.
- [22] N. Hautière, J.-P. Tarel, D. Aubert, and É. Dumont, "Blind contrast enhancement assessment by gradient ratioing at visible edges," *J. Image Anal. Stereol.*, vol. 27, no. 2, pp. 87–95, Jun. 2008.
- [23] C. O. Ancuti, C. Ancuti, C. Hermans, and P. Bekaert, "A fast semi-inverse approach to detect and remove the haze from a single image," in *Proc. Asian Conf. Comput. Vis.*, 2010, pp. 501–514.
- [24] Q. Zhang and S.-I. Kamata, "Improved optical model based on region segmentation for single image haze removal," *Int. J. Inform. Electron. Eng.*, vol. 2, no. 1, pp. 62–68, Jan. 2012.
- [25] D. L. Ruderman, "The statistics of natural images," *Netw., Comput. Neural Syst.*, vol. 5, no. 4, pp. 517–548, 1994.
- [26] A. Mittal, A. K. Moorthy, and A. C. Bovik, "No-reference image quality assessment in the spatial domain," *IEEE Trans. Image Process.*, vol. 21, no. 12, pp. 4695–4708, Dec. 2012.
- [27] A. Mittal, R. Soundararajan, and A. C. Bovik, "Making a 'completely blind' image quality analyzer," *IEEE Signal Process. Lett.*, vol. 20, no. 3, pp. 209–213, Mar. 2013.
- [28] I. I. A. Groen, S. Ghebreab, H. Prins, V. A. F. Lamme, and H. S. Scholte, "From image statistics to scene gist: Evoked neural activity reveals transition from low-level natural image structure to scene category," *J. Neurosci.*, vol. 33, no. 48, pp. 18814–18824, Nov. 2013.
- [29] C. E. Shannon, "A mathematical theory of communication," *Bell Syst. Tech. J.*, vol. 27, no. 3, pp. 379–423, 1948.
- [30] D. Hasler and S. E. Suesstrunk, "Measuring colorfulness in natural images," *Proc. SPIE*, vol. 5007, pp. 87–95, Jun. 2003.
- [31] R. O. Duda, P. E. Hart, and D. G. Stork, *Pattern Classification*. New York, NY, USA: Wiley, 2012.
- [32] L. K. Choi, J. You, and A. C. Bovik, "Referenceless perceptual image defogging," in *Proc. IEEE Southwest Symp. Image Anal. Interpretation*, Apr. 2014, pp. 165–168.
- [33] B. Qi, T. Wu, and H. He, "A new defogging method with nested windows," in *Proc. IEEE Int. Conf. Inf. Eng. Comput. Sci.*, Dec. 2009, pp. 1–4.
- [34] W. S. Geisler, "Visual perception and the statistical properties of natural scenes," *Annu. Rev. Psychol.*, vol. 59, pp. 167–192, Jan. 2008.
- [35] E. P. Simoncelli and B. A. Olshausen, "Natural image statistics and neural representation," *Annu. Rev. Neurosci.*, vol. 24, pp. 1193–1216, May 2001.
- [36] M. Carandini, D. J. Heeger, and J. A. Movshon, "Linearity and normalization in simple cells of the macaque primary visual cortex," *J. Neurosci.*, vol. 17, no. 21, pp. 8621–8644, 1997.
- [37] M. J. Wainwright, O. Schwartz, and E. P. Simoncelli, "Natural image statistics and divisive normalization: Modeling nonlinearities and adaptation in cortical neurons," in *Statistical Theories of the Brain*. Cambridge, MA, USA: MIT Press, 2002, pp. 203–222.
- [38] L. K. Choi, J. You, and A. C. Bovik, "Referenceless perceptual fog density prediction model," *Proc. SPIE*, vol. 9014, p. 90140H, Feb. 2014.
- [39] A. A. Michelson, *Studies in Optics*. Chicago, IL, USA: Univ. Chicago Press, 1927.
- [40] H. S. Scholte, S. Ghebreab, L. Waldorp, A. W. Smeulders, and V. A. Lamme, "Brain responses strongly correlate with Weibull image statistics when processing natural images," *J. Vis.*, vol. 9, no. 4, pp. 29.1–29.15, Apr. 2009.
- [41] D. C. Marr and E. Hildreth, "Theory of edge detection," *Proc. Roy. Soc. London B, Biol. Sci.*, vol. 207, no. 1167, pp. 187–217, 1980.
- [42] D. J. Heeger, "Normalization of cell responses in cat striate cortex," *Vis. Neurosci.*, vol. 9, no. 2, pp. 181–197, 1992.
- [43] M. Clark and A. C. Bovik, "Experiments in segmenting texton patterns using localized spatial filters," *Pattern Recognit.*, vol. 22, no. 6, pp. 707–717, 1989.
- [44] *Studio Encoding Parameters of Digital Television for Standard 4:3 and Wide-Screen 16:9 Aspect Ratio*, document ITU BT-601-5, 1995.
- [45] M. D. Fairchild, *Color Appearance Models*. New York, NY, USA: Wiley, 2005.
- [46] A. C. Bovik, "Perceptual image processing: Seeing the future," *Proc. IEEE*, vol. 98, no. 11, pp. 1799–1803, Nov. 2010.
- [47] H. R. Sheikh, M. F. Sabir, and A. C. Bovik, "A statistical evaluation of recent full reference image quality assessment algorithms," *IEEE Trans. Image Process.*, vol. 15, no. 11, pp. 3440–3451, Nov. 2006. [Online]. Available: [live.ece.utexas.edu/research/quality/subjective.htm](http://live.ece.utexas.edu/research/quality/subjective.htm)
- [48] D. Martin, C. Fowlkes, D. Tal, and J. Malik, "A database of human segmented natural images and its application to evaluating segmentation algorithms and measuring ecological statistics," in *Proc. IEEE Int. Conf. Comput. Vis.*, Jul. 2001, pp. 416–423. [Online]. Available: <http://www.eecs.berkeley.edu/Research/Projects/CS/vision/bsds/>
- [49] P. L. Callet and F. Atrusseau. (2005). *Subjective Quality Assessment IRCCyN/IVC Database*. [Online]. Available: <http://www.irccyn.ec-nantes.fr/ivcd/>
- [50] E. C. Larson and D. M. Chandler, "Most apparent distortion: Full-reference image quality assessment and the role of strategy," *J. Electron. Imag.*, vol. 19, no. 1, p. 011006, 2010. [Online]. Available: [vision.okstate.edu/?loc=csiq](http://vision.okstate.edu/?loc=csiq)
- [51] Flickr. [Online]. Available: <http://www.flickr.com>, accessed Jan. 2014.
- [52] G. D. Finlayson and E. Trezzi, "Shades of gray and colour constancy," in *Proc. 12th Color Imag. Conf.*, 2004, pp. 37–41.
- [53] R. Achanta, S. Hemami, F. Estrada, and S. Süsstrunk, "Frequency-tuned salient region detection," in *Proc. IEEE Conf. Comput. Vis. Pattern Recognit.*, Jun. 2009, pp. 1597–1604.
- [54] A. Saleem, A. Beghdadi, and B. Boashash, "Image fusion-based contrast enhancement," *EURASIP J. Image Video Process.*, vol. 2012, no. 1, pp. 1–17, 2012.
- [55] P. J. Burt and E. H. Adelson, "The Laplacian pyramid as a compact image code," *IEEE Trans. Commun.*, vol. 31, no. 4, pp. 532–540, Apr. 1983.
- [56] D. H. Brainard, "The psychophysics toolbox," *Spatial Vis.*, vol. 4, no. 4, pp. 433–436, 1997.
- [57] *Methodology for the Subjective Assessment of the Quality of Television Pictures*, document ITU BT-500-11, 2002.
- [58] F. Guo, J. Tang, and Z.-X. Cai, "Objective measurement for image defogging algorithms," *J. Central South Univ.*, vol. 21, no. 1, pp. 272–286, 2014.



**Lark Kwon Choi** (M'14) received the B.S. degree in Electrical Engineering from Korea University, Seoul, Korea, and the M.S. degree in Electrical Engineering and Computer Science from Seoul National University, Seoul, Korea, in 2002 and 2004, respectively. From 2004 to 2009, he was with KT, Seoul, Korea, as a Senior System Engineer, on Internet-protocol-television (IPTV) platform research and development. He has contributed to IPTV standardization in International Telecommunication Union Telecommunication Standardization Sector, Internet Engineering Task Force, and Telecommunications Technology Association.

He is currently pursuing the Ph.D. degree as a member of the Laboratory for Image and Video Engineering and the Wireless Networking and Communications Group at The University of Texas at Austin, Austin, TX, under the supervision of Dr. A. C. Bovik. His research interests include image and video quality assessment, spatial and temporal visual masking, motion perception, and perceptual image and video quality enhancement.



**Jaehye You** received the B.S. degree in Electronics Engineering from Seoul National University, Seoul, Korea, in 1985, and the M.S. and Ph.D. degrees in Electrical Engineering from Cornell University, Ithaca, NY, in 1987 and 1990, respectively. In 1990, he joined Texas Instruments, Dallas, TX, as a Member of Technical Staff. In 1991, he joined the School of Electrical Engineering, Hongik University, Seoul, Korea, as a faculty member, where he is currently supervising the Semiconductor Integrated System Laboratory. He has served as an

Executive Director of the Drive technology and System Research Group, Korean Information Display Society. His current research interests include integrated system design for display image signal processing, image-based home networking, and perceptual image quality enhancement systems.

He was a recipient of the Korean Ministry of Strategy and Finance, KEIT Chairman Award for Excellence, in 2011. He is also an Associate Editor of the *Journal of Information Display*. He was a Technical Consultant for various companies, such as Samsung Semiconductor, SK Hynix, Global Communication Technologies, P&K, Penta Micro, and Primenet.



**Alan Conrad Bovik** (F'96) is currently the Cockrell Family Endowed Regents Chair of Engineering with The University of Texas at Austin, where he is the Director of the Laboratory for Image and Video Engineering. He is a Faculty Member with the Department of Electrical and Computer Engineering and the Institute for Neuroscience. He has authored over 750 technical articles in these areas, and holds several U.S. patents. His publication have been cited over 43000 times in the literature, his current H-index of 75, and he is listed as a Highly-Cited

Researcher by Thompson Reuters. His several books include the companion volumes *The Essential Guides to Image and Video Processing* (Academic Press, 2009). His research interests include image and video processing, computational vision, and visual perception.

He has received a number of major awards from the IEEE Signal Processing Society, including: the Society Award (2013); the Technical Achievement Award (2005); the Best Paper Award (2009); the Signal Processing Magazine Best Paper Award (2013); the Education Award (2007); the Meritorious Service Award (1998), and (co-author) the Young Author Best Paper Award (2013). He was also a recipient of the Honorary Member Award of the Society for Imaging Science and Technology for 2013, the SPIE Technical Achievement Award for 2012, and was the IS&T/SPIE Imaging Scientist of the Year Award for 2011. He is also a recipient of the Hocott Award for Distinguished Engineering Research, and the Joe J. King Award for Professional Achievement (2015), from The University of Texas at Austin (2008), and the Distinguished Alumni Award from the University of Illinois at Champaign-Urbana (2008). He is a fellow of the Optical Society of America, and the Society of Photo-Optical and Instrumentation Engineers. He cofounded and was the longest-serving Editor-in-Chief of the IEEE TRANSACTIONS ON IMAGE PROCESSING (1996-2002); created and served as the first General Chair of the IEEE International Conference on Image Processing, held in Austin, TX, in November, 1994, along with numerous other professional society activities, including the Board of Governors of the IEEE Signal Processing Society (1996-1998), the Editorial Board of THE PROCEEDINGS OF THE IEEE (1998-2004), and a Series Editor for *Image, Video, and Multimedia Processing* (Morgan and Claypool Publishing Company) (2003-present). He was also the General Chair of the 2014 Texas Wireless Symposium, held in Austin, in 2014. He is a registered Professional Engineer in the State of Texas, and is a frequent consultant to legal, industrial, and academic institutions.